Role of Latent Heating Vertical Distribution in the Formation of the Tropical Cold Trap

Kai-Wei Chang[1] [ID] and **Tristan S. L'Ecuyer[1]** [ID]

[1]Department of Atmospheric and Oceanic Sciences, University of Wisconsin-Madison, Madison, WI, USA

Abstract This study examines the role of latent heating (LH) vertical distribution in tropical tropopause layer (TTL) cooling and upper-tropospheric warming associated with equatorial wave responses using LH from the Tropical Rainfall Measurement Mission and temperature from radio occultation observations. We distinguish the effects of convective and stratiform LH in tropical convection on temperature in the upper troposphere and lower stratosphere. Cross-spectral analysis of time series of temperature and LH shows that stratiform LH exhibits higher coherence with temperature throughout most of the upper troposphere and lower stratosphere, especially in the equatorial Rossby wave response. Coherence between total LH and temperature tends to increase with the altitude of heating. Highest coherences occur almost exclusively at time scales of the Madden-Julian Oscillation, suggesting the importance of mesoscale convective activity in TTL cooling and subsequent dehydration processes. These results demonstrate that TTL and upper-tropospheric temperature perturbations depend on the vertical distribution of LH and that stratiform LH release has strong relationship with the formation of the horseshoe-shaped cold trap over the Maritime Continent and West Pacific.

1. Introduction

Stratospheric water vapor exerts a strong control on climate (Forster & Shine, 1999) as its increase cools the stratosphere, warms global surface temperatures (Rind & Lonergan, 1995), and plays a key role in the removal of ozone by polar stratospheric clouds (Solomon et al., 1986). The water vapor mixing ratio of air entering the stratosphere is strongly controlled by temperature in the tropical tropopause layer (TTL), as seen through the "tape-recorder" signal (Mote et al., 1996), in which the seasonal cycle of TTL temperature is imprinted onto the water vapor upwelling into the lower stratosphere. As such, understanding processes that control TTL temperatures is crucial for studying climate and stratospheric chemistry.

TTL conditions near the Maritime Continent (MC) are particularly important since this region is a major pathway of troposphere-to-stratosphere transport (Fueglistaler, 2005). During boreal winter, a cold trap or temperature minimum resembling a horseshoe forms over the MC region, as seen in the climatological temperature distribution (Figure 1). It is clear that this cold pattern coincides with low water vapor concentration and high cirrus frequency, indicative of the dehydration process via cirrus formation (Jensen et al., 1996). The distributions of these properties are also dependent on the phase of the El Niño–Southern Oscillation, with the horseshoe shape shifted westward closer to the MC during La Niña phases. This dependence on El Niño–Southern Oscillation phase depicts the influence of tropospheric circulation on the formation of the horseshoe cold region.

The horseshoe-shaped morphology is thought to result from the Matsuno-Gill response to tropospheric diabatic heating (Highwood & Hoskins, 1998), which excites a stationary Kelvin wave (KW) to the east of the heating and stationary equatorial Rossby wave (ERW) to the west of the heating (Figure 2; Gill, 1980; Matsuno, 1966). The cold region associated with the KW response is centered on the equator, while the RW cooling responses are off the equator into each hemisphere, forming the tail of the horseshoe. Studies have demonstrated that intraseasonal variability of TTL temperature, especially in the MC region, is strongly modulated by ERW and KW associated with convective activity, for instance, through analysis of outgoing longwave radiation (Nishimoto & Shiotani, 2012; Zhou & Holton, 2002) and cloud top height (Kim et al., 2018; Paulik & Birner, 2012). Both are proxies of convective strength, but neither can resolve the vertical distribution of heating. Modeling studies (e.g., Ryu et al., 2008) imposing a heating source on atmospheric flow also show that planetary waves cause significant temperature perturbations in the MC region, but the
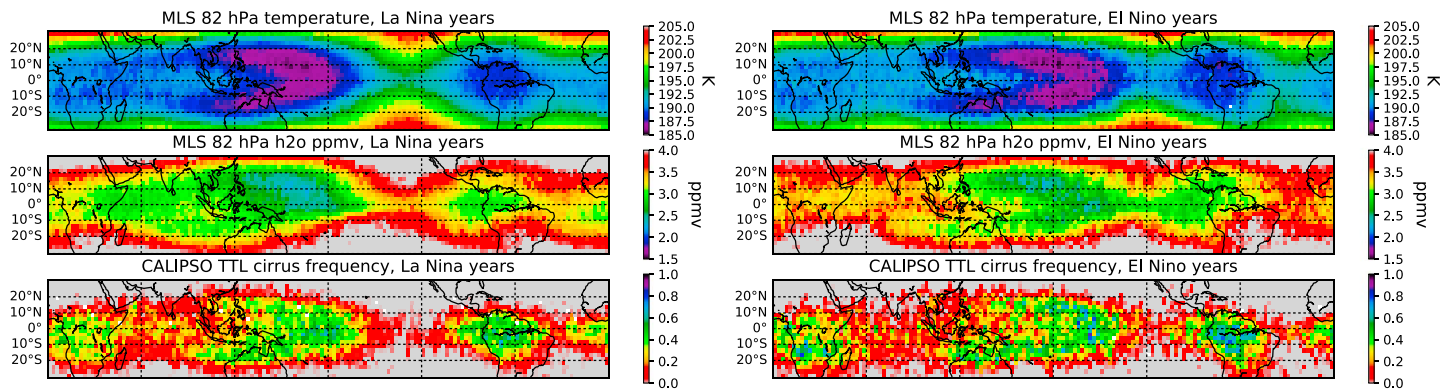
Figure 1. December-January-February (DJF) climatology of 82-hPa temperature (top row) and water vapor concentration (middle row) retrieved by the Aura Microwave Limb Sounder and frequency of cirrus clouds with cloud base above 15 km (bottom row) based on the CALIPSO 5-km cloud layer product. The left column shows composites on DJF periods with the Oceanic Niño Index < −0.5 (2008, 2009, 2011, and 2012), and those on the right correspond to DJF periods with Oceanic Niño Index > 0.5 (2007 and 2010). TTL = tropical tropopause layer.

role of variations in the heating vertical distribution has not been quantitatively assessed. Since the stationary planetary waves are caused by diabatic heating (Gill, 1980) and mass flux into the layer (Matsuno, 1966), physically, it is plausible to expect that the horseshoe-shaped cold region depends somewhat on the vertical distribution of heating. However, it remains poorly understood whether properties of these waves are related to the specific vertical configuration of heating.

Since tropospheric diabatic heating is dominated by latent heating (LH) from precipitation, it is reasonable to anticipate that the shape and intensity of the cold trap is linked to mesoscale convective systems (MCS), which contribute to more than half of tropical rainfall (Nesbitt et al., 2006). Convective precipitation forms during the early stage of storm development, and as the MCS matures, a large area of outflow forms, and in it, the weak updrafts form significant amounts of stratiform precipitation (Houze, 2004). The mean profiles of convective and stratiform LH over the MC region (Figure 3) show the typical vertical distribution of LH from these two precipitation regimes. While the LH from convective precipitation is positive throughout the atmosphere and peaks in the lower troposphere, stratiform precipitation forms higher in the troposphere, resulting in higher LH peaks. In addition to the heating aloft, stratiform LH is characterized by cooling below the melting layer due to evaporation. The combination of radar measurements and cloud-resolving models makes it possible to separate the two components of heating (Tao et al., 2010), and we take advantage of this capability to investigate whether these two types of LH relate differently to temperatures in the upper troposphere and lower stratosphere (UTLS). Together with the high vertical resolution of temperature profiles from radio occultation (RO) observations (Kursinski et al., 1997), these data sets also give insight into the vertical structure of the temperature responses.
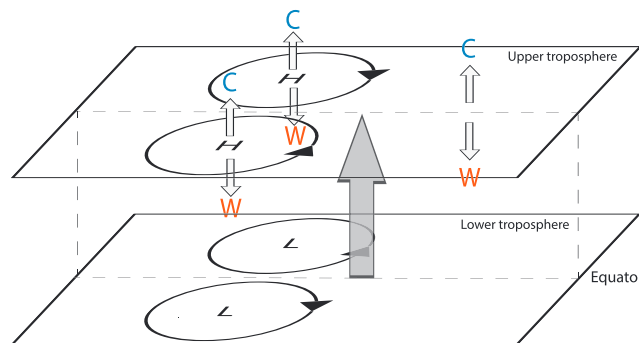

Figure 2. Schematic of circulation and temperature anomaly induced by tropospheric heating at the location indicated by the bold gray arrow in an resting atmosphere. High- and low-pressure anomalies are indicated by H and L, respectively, while cold and warm anomalies are indicated by blue C and orange W letters. Adapted from Highwood and Hoskins (1998).
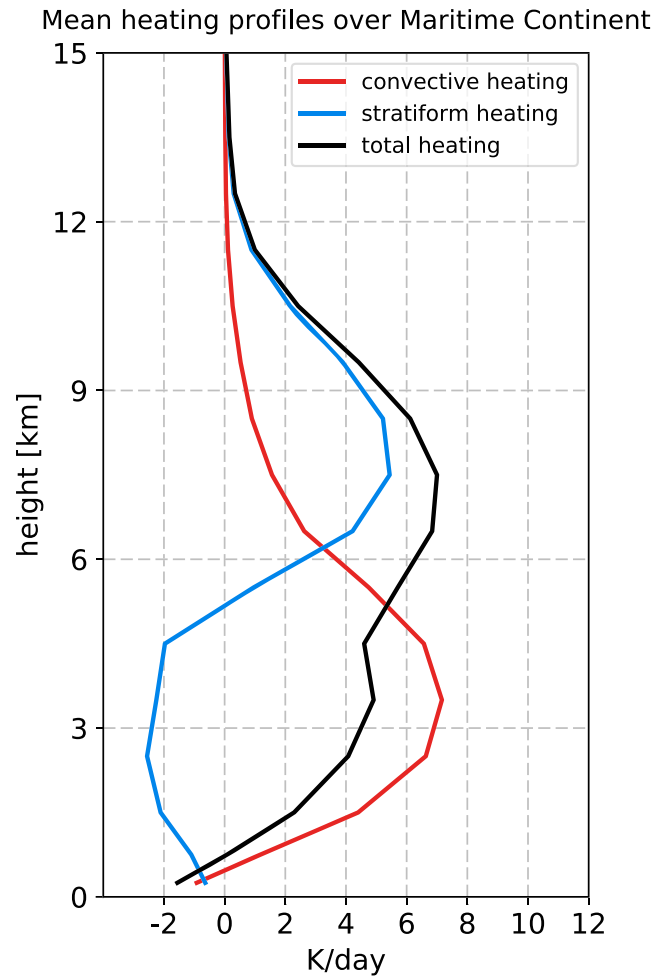
Figure 3. Mean convective (red), stratiform (blue), and total (black) latent heating profiles within a box over the Maritime Continent ($\pm10°$N/S and 110–150°E), calculated using the Tropical Rainfall Measurement Mission Spectral Latent Heating product over years 2006–2014.

To understand how the variability of tropical UTLS temperature relates to the height of tropical LH, we study the time series of convective and stratiform LH extracted from the Tropical Rainfall Measurement Mission (TRMM) Spectral LH (SLH) product (Shige et al., 2004) and temperature derived from RO observations. Through cross-spectral analysis, we show that throughout most of the upper troposphere and the TTL, temperature variations are more coherent with stratiform heating rather than convective heating and exhibit a dependence on the altitude of total heating. The phase lags of statistically significant coherences show that the temperature variability has a vertical structure consistent with ERW/KW as described by previous studies. The lags between temperature and LH generally fall within 0 to 14 days, consistent with the time scale of ERW/KW evolution found in Jin and Hoskins (1995). Results also show that the level at which the temperature perturbation switches from warming to cooling is near 150 hPa (warming below and cooling above), consistent with Dima and Wallace (2007) who found that the strongest geopotential height and wind perturbations occur near this altitude. Finally, largest coherences occur almost exclusively at time scales corresponding to the Madden-Julian Oscillation (MJO), suggesting the importance of MCS activity in TTL cooling and subsequent dehydration processes, which has also been suggested by Kim, Randel, and Birner (2018).

A description of the satellites and retrieval products utilized in this study is given in section 2. Section 3 explains the construction of LH and temperature time series, processing of the time series, the cross-spectral analysis, and significance testing. We present the results of the analysis in section 4 and give a summary and discuss implications of this study in section 5.
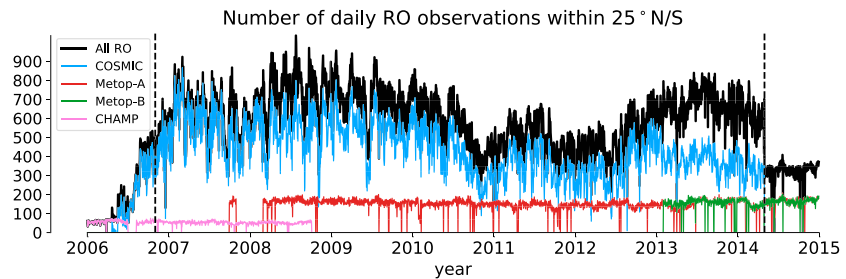
Figure 4. Daily count of wetPrf profiles within 25°N/S from each RO mission. Dashed lines indicate the beginning and end of the period used in this study. RO = radio occultation; COSMIC = Constellation Observation System for Meteorology, Ionosphere, and Climate; Metop = Meteorological Operational Polar Satellite; CHAMP = Challenging Minisatellite Payload.

2. Data

2.1. Temperature From RO

This study uses the reprocessed RO data sets processed by the Cosmic Data Analysis and Archive Center, which include occultations from the following satellite missions: Constellation Observation System for Meteorology, Ionosphere, and Climate (Anthes et al., 2008), Meteorological Operational Polar Satellite A/Global Navigation Satellite System Receiver for Atmospheric Sounding (Von Engeln et al., 2009), Meteorological Operational Polar Satellite B/Global Navigation Satellite System Receiver for Atmospheric Sounding, and the Challenging Minisatellite Payload (Wickert et al., 2001). Because the RO technique does not suffer from intersatellite calibration effects (Foelsche et al., 2011), profiles from different satellite missions can be used together as long as they are processed with the same algorithm. Temperatures from 500 to 70 hPa are taken from the level 2 wetPrf products of the above missions. Although wetPrf profiles provide temperature every 100 m, the effective vertical resolution of the RO technique is around 1 km near the tropopause (Kursinski et al., 1997). Precision of temperature from RO is approximately 0.5 K within altitudes of 8 to 20 km (Anthes et al., 2008). Figure 4 show the daily count of wetPrf profiles available within 25° of the equator.

2.2. LH From TRMM

The TRMM was launched in 1997 to improve our understanding of tropical precipitation and LH (Kummerow et al., 1998; Simpson et al., 1988). Its Precipitation Radar (PR) observes the vertical structure of clouds and enables the retrieval of vertically resolved LH in clouds. This study uses the SLH product (Shige et al., 2004, 2007, 2008, 2009) within the time period of 2006 to 2014, when there was an abundance of RO observations.

The SLH algorithm employs a lookup table approach to retrieve LH. Lookup tables were generated with the Goddard Cumulus Ensemble model (Tao & Simpson, 1993) by simulating the LH structures based on observations of the Tropical Ocean and Global Atmosphere Coupled Ocean-Atmosphere Response Experiment (Shige et al., 2004). Global applicability of these lookup tables were evaluated with observations from various other campaigns (Shige et al., 2007). Simulated scenes are categorized as convective, shallow stratiform, or deep stratiform (anvil) based on precipitation rate, cloud water, and updraft velocity of the model grid point as well as surrounding gridpoints; details of the separation method are given in Section 3a of Shige et al. (2004). Inputs for the lookup table include precipitation-top height, precipitation rate, and precipitation type (convective or stratiform). To retrieve the LH of TRMM PR observations, the precipitation-top height and precipitation rates from the 2A25 product (Iguchi et al., 2000) and precipitation type from the 2A23 product (Awaka et al., 2002; Schumacher & Houze, 2003) were used. The method of precipitation type identification using the PR is based on the identification of the bright band from the melting layer and the vertical distribution of radar reflectivity.

Hagos et al. (2010) conducted a comparison of LH among reanalyses, various TRMM algorithms (including SLH), and sounding-based estimates. They show that the structure of the deep modes are similar across data sets in different tropical regions, while the shallow modes differ significantly. Tao et al. (2016) show that the SLH better resolves shallow convection (see their Figures 2–4) compared to the Goddard Convective-Stratiform Heating algorithm (Tao et al., 1993). Total heating estimates from existing TRMM LH algorithms generally compare well with sounding-based estimates (Figures 2-5 and 2-7 of Tao et al., 2016),
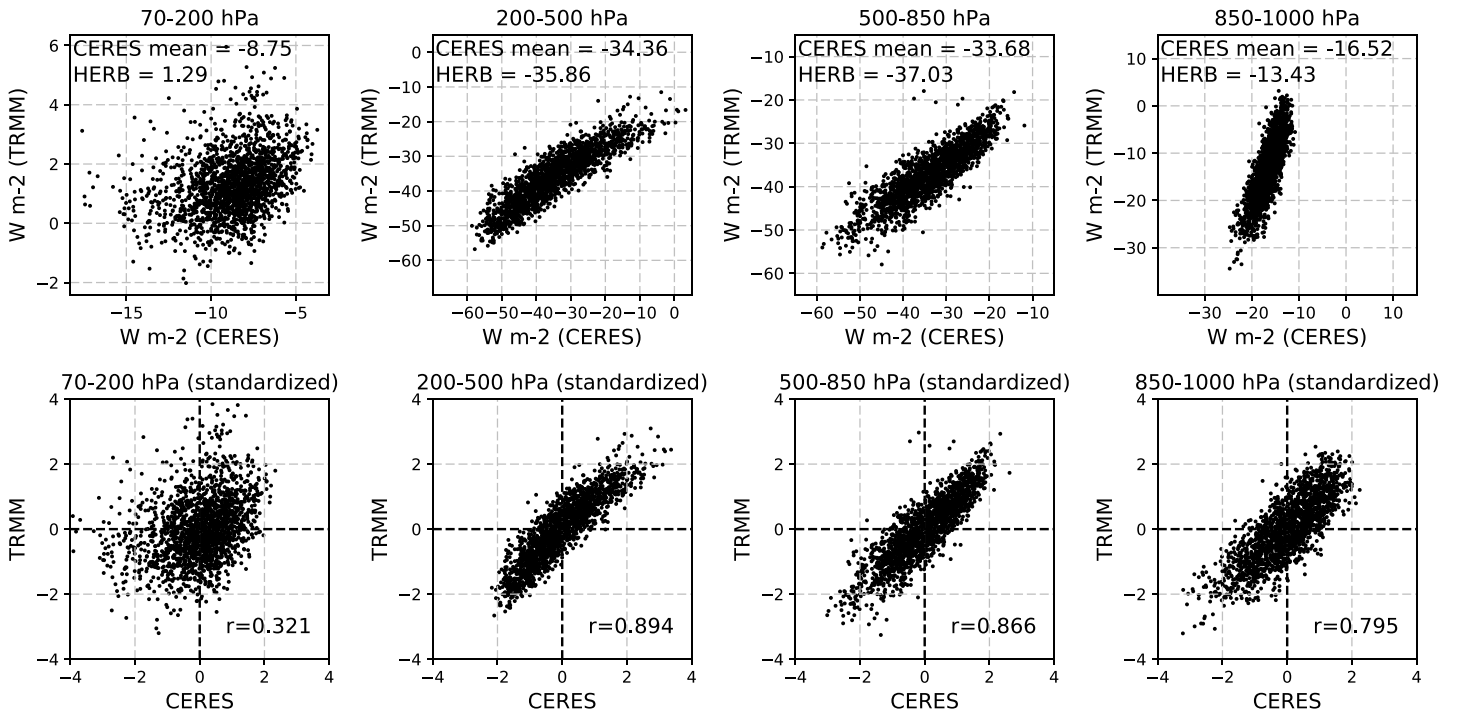
Figure 5. Scatterplot of vertically integrated Q_R inside the Indian Ocean Center box (Figure 7) estimated from the CERES SYN1deg and TRMM HERB product. Each dot represents daily mean values inside the box. Top row shows values in physical units (W/m^2), with the mean value of each data set denoted in the legend. The bottom row is in standardized space, with the correlation coefficient r denoted. CERES = Clouds and the Earth's Radiant Energy System; HERB = Hydrologic Cycle and Earth's Radiation Budget; TRMM = Tropical Rainfall Measurement Mission.

with some differences in amplitude and vertical structure. However, we note that the reliability of the separate convective and stratiform components is not well documented, since validations using soundings have generally been focused on total heating.

SLH provides estimates of pure LH as well as $Q_1 - Q_R$, the difference between the apparent heating Q_1 (Yanai et al., 1973) and the radiative heating Q_R, which we will refer to as Q_{1R}. The Q_1 is the sum of LH, radiative heating, and vertical convergence of vertical eddy transport of heat flux. Since the last two terms are typically much smaller relative to LH, Q_{1R} is very close to LH (Shige et al., 2004). Since there are no Q_R estimates based on TRMM that covers the entirety of 2006–2014, in this study we use Q_{1R} in the main analysis, and Q_R is treated separately as described below. In the following discussions, we use the term LH in reference to Q_{1R}.

2.3. Radiative Heating From CERES and Its Consistency With TRMM Estimates

To estimate Q_R, we use the Clouds and the Earth's Radiant Energy System (CERES) SYN1deg daily product (Doelling et al., 2016) which provides shortwave and longwave fluxes at levels 1,000, 850, 500, 200, and 70 hPa and top-of-atmosphere. Q_R at layers between 1,000 and 850 hPa, 850 and 500 hPa, 500 and 200 hPa, and 200 and 70 hPa are calculated from these fluxes. Cloud information in the SYN1deg algorithm comes from a combination of observations from the Moderate Resolution Imaging Spectroradiometer (MODIS) and geostationary satellites. Estimates of radiative heating from TRMM are also available from the Hydrologic Cycle and Earth's Radiation Budget (HERB) data set (L'Ecuyer & Mcgarragh, 2010) for the period 1998 to 2010. However, this overlaps with only about half of the Constellation Observation System for Meteorology, Ionosphere, and Climate data record (2007–2014). For this reason, we use HERB only to check the consistency of Q_R estimates between CERES and TRMM, as discussed below.

Q_R is vertically integrated in the layers 1,000–850, 850–500, 500–200, and 200–70 hPa for both the CERES SYN1deg and TRMM HERB data sets. Following Yanai et al. (1973), the vertically integrated heating of the ith layer, $\overline{Q^{(i)}}$, is calculated as

$$\overline{Q^{(i)}} = \frac{1}{g} \int_{p_{\text{top}}^{(i)}}^{p_{\text{base}}^{(i)}} Q(p)\,\mathrm{d}p, \qquad (1)$$
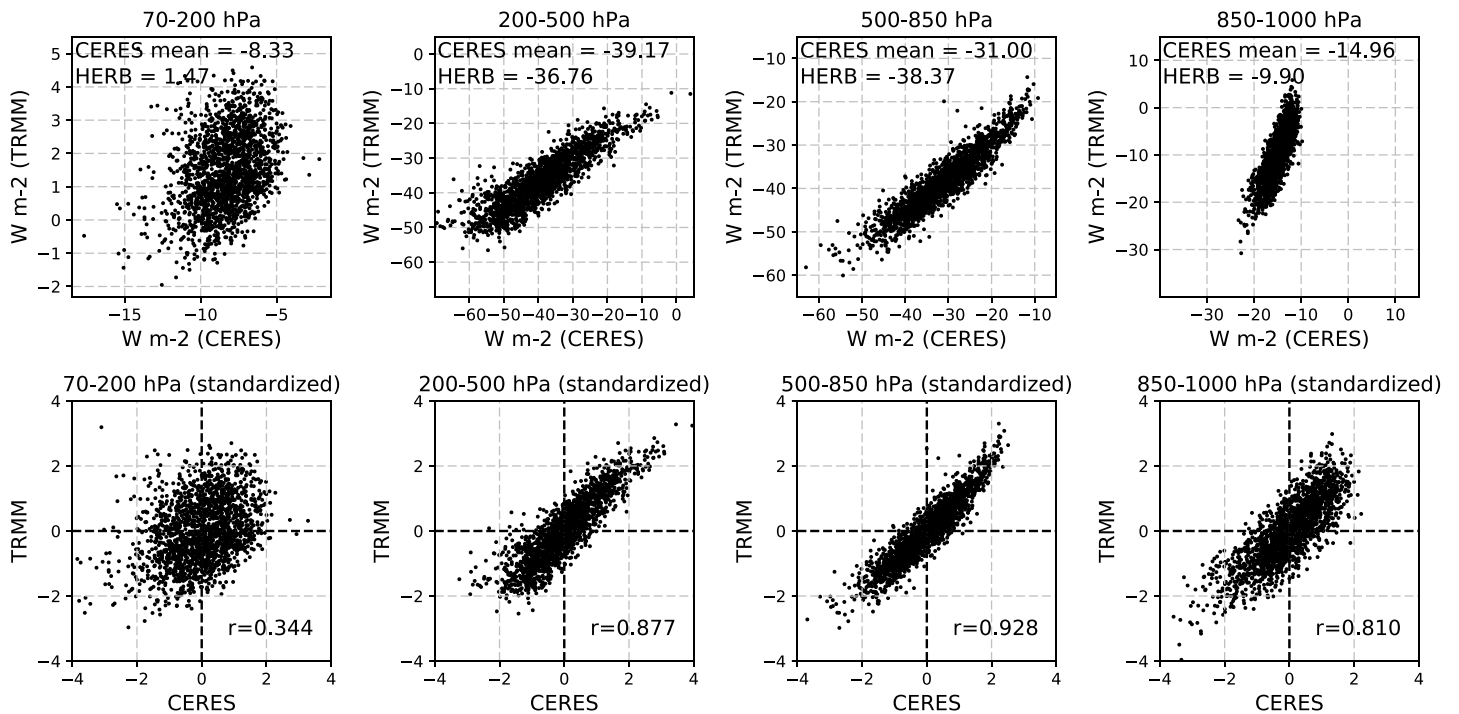
Figure 6. Same as Figure 5 except for the Maritime Continent Center box.

where g is the gravitational acceleration, $Q(p)$ is the profile of heating as a function of pressure p, and p_{top} and p_{base} are the pressure of the top and bottom of the ith layer. Figures 5 and 6 show comparisons of integrated Q_R over the Indian Ocean (IO) and MC region. Aside from the 70- to 200-hPa layer, correlation coefficients between the two data sets are high (0.795 or greater), showing the consistency of Q_R between CERES and TRMM estimates. The low correlation in the 70- to 200-hPa layer may be due to the effects of high clouds.

3. Time Series Processing and Cross-Spectral Analysis

3.1. Construction and Preprocessing of Time Series

Time series of daily mean temperature and LH from 1 November 2006 to 30 April 2014 (dashed lines in Figure 4) are constructed in the boxes shown in Figure 7. We designate two areas of study, one over the IO and another over the MC. In each area, one box centered on the equator is used to construct the LH time series, and the North, South, East, and Center boxes are used to construct time series of temperature. The locations of the North and South boxes coincide the location of the ERW response, while the East boxes coincide with the KW response. Note that, as shown in Figure 2, the anticyclones are slight westward of heating. This is the pattern of the stationary ERW in a resting atmosphere, and Jin and Hoskins (1995) shows that in realistic atmospheric flow, the anticyclones almost flank the heating directly north and south. For this reason, the North and South boxes are placed directly north and south of the heating boxes. The relationship between the temperature time series inside the (IO,MC) North, South, East, and Center boxes and the LH time series in the (IO,MC) Center boxes is analyzed through cross-spectral analysis.

Time series of temperature are made at 500, 400, 350, 300, 250, 200, 170 hPa and every 10 hPa between 150 and 70 hPa. For LH, we split the atmosphere into the following layers: 0–3, 3–6, 6–9, 9–12, and 12–15 km, and Q_{1R} is integrated in these layer using equation (1) to represent the vertically integrated LH.

Heating above 15 km is negligible (Figure 3) and is omitted. The same integrated quantity is calculated for convective LH, stratiform LH, and total (sum of convective and stratiform) LH. All time series are first deseasonalized by removing the sinusoidal variations from the first three harmonics of the annual cycle and then standardized prior to performing the cross-spectral analysis.

Time series of Q_R based on CERES SYN1deg estimates are constructed in the same manner as above, except the vertical layers are 1,000–850, 850–500, 500–200, and 200–70 hPa instead of the 3-km layers. Due to the
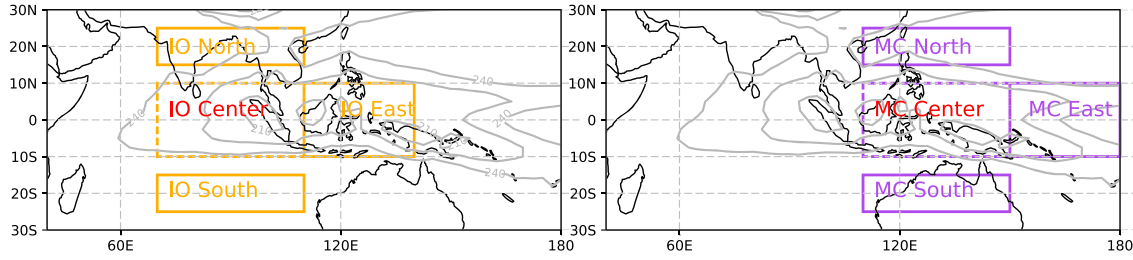
Figure 7. Boxes in which temperature and heating time series are constructed. The latent heating time series are constructed inside the IO Center and MC Center boxes labeled in red, while temperature time series are constructed in the IO/MC North, South, East, and Center boxes. Contours at intervals of 15 W/m^2 are mean outgoing longwave radiation through 2006–2014 derived from the National Oceanic and Atmospheric Administration Interpolated Outgoing Longwave Radiation daily data set. IO = Indian Ocean; MC = Maritime Continent.

differences in vertical resolution and spatial sampling between TRMM and CERES, Q_R is not added to the Q_{1R} term, and cross-spectral analysis is performed separately on Q_R and Q_{1R}.

3.2. Cross-Spectral Analysis and Significance Testing

Cross-spectral analysis is used to examine the relationship between two time series in the frequency domain. The *coherence spectrum* is analogous to the correlation coefficient and gives a measure of how closely two time series are varying together at a frequency f, while the *phase spectrum* tells whether one time series is leading or lagging the other at f. Given two time series x, y, their power spectral densities $P_{xx}(f), P_{yy}(f)$, and the cross-spectral density $P_{xy}(f)$, the coherence (or coherence-squared) spectrum is

$$Coh^2(f) = |r_{xy}(f)|^2 = \frac{|P_{xy}(f)|^2}{P_{xx}(f)P_{yy}(f)}, \tag{2}$$

and the phase spectrum is

$$\theta_{xy}(f) = \tan\left[\frac{Im(r_{xy})}{Re(r_{xy})}\right]. \tag{3}$$

The coherence falls between 0 and 1, where a value of 1 indicates that at f the amplitudes of the two time series are linearly related.

The cross-spectral densities are estimated using Welch's (1967) average periodogram method. Estimates of effective degree of freedom (eDOF) and the choice of window length for the spectral density estimation follow Biltoft and Pardyjak (2009). The eDOF is calculated as $(8/3)N/nfft$ where N is the length of the time series and *nfft* is the width of window used to calculated the power densities. Although the length of each time series is $N = 2,738$ days, each day cannot be seen as independent. The number of independent samples is calculated by (Bretherton et al., 1999)

$$N*= N\left[\frac{1 - r_x r_y}{1 + r_x r_y}\right], \tag{4}$$

where r_x and r_y are the lag-one autocorrelation of x and y. Biltoft and Pardyjak (2009) recommends that the eDOF fall within 10 to 100 for reliable significance testing. By using values $nfft = 128$ and an overlap of 64, most of the eDOFs fall within 40 to 60, which is in the recommended range.

Significance testing of coherence also follows Biltoft and Pardyjak (2009). A coherence value is statistically significant at the $(1 - p) \times 100\%$ level if it is greater than the value calculated from

$$\chi_{1-p} = \frac{2F_p}{\text{eDOF} - 2 - 2F_p}, \tag{5}$$

where F_p is the value of the $F(2, \text{eDOF} - 2)$ distribution at $1 - p$. All significant levels shown in the results are calculated with $p = 0.01$ (99% significance).
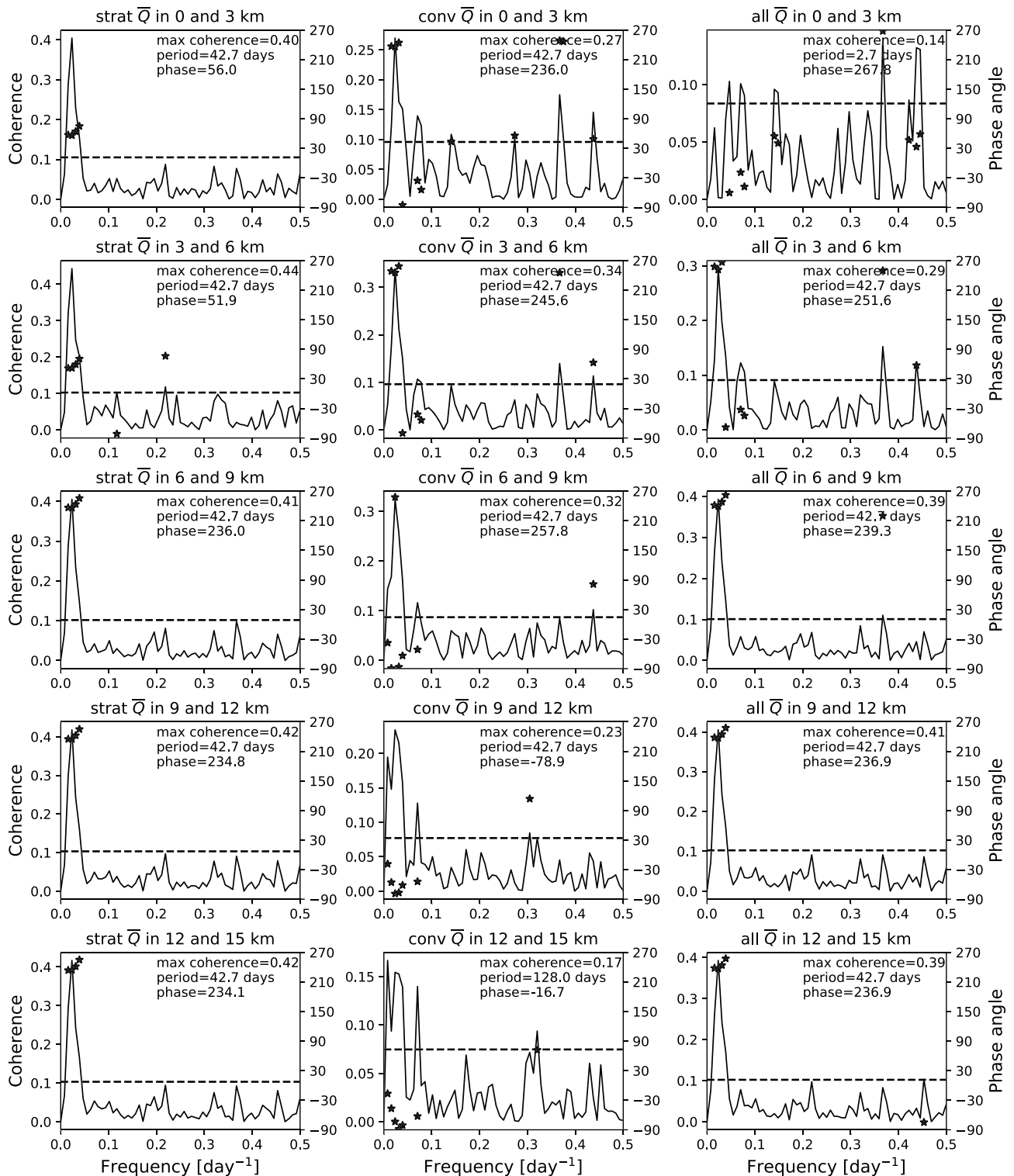
Figure 8. Coherence spectra between 100-hPa mean temperature inside Indian Ocean South (see Figure 7) and stratiform (left column), convective (middle column), and total (right column) heating inside Indian Ocean Center in the five vertical layers defined in section 3. Dashed lines indicate the significant coherence at the 99% level. Phases for coherences above this level are plotted as stars. The max coherence in each case and the corresponding period and phase are summarized in the legends.
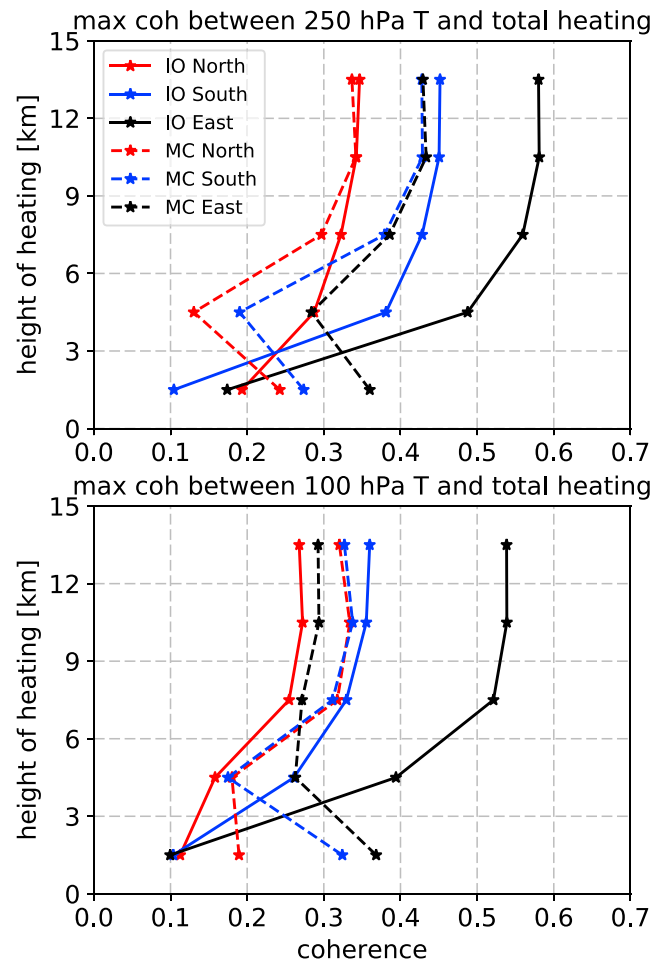
Figure 9. Maximum coherence between total heating at each of the five layers and temperature at 250 hPa (top) or 100 hPa (bottom). The maximum coherence represents the highest value of the coherence spectrum (see Figure 8) out of all frequencies. IO = Indian Ocean; MC = Maritime Continent.

4. Results

Figure 8 shows the coherence spectra between 100 hPa average temperature in IO South and convective, stratiform, or total LH inside the IO heating box in the five layers as defined in the methodology. Since Figure 8 shows only one altitude of temperature over one location, this plot serves simply as an example of the coherence and phase spectrum. The results below are based on similar analyses of the gross features of the coherences and phases from all levels of temperature and all locations.

Although we evaluate the LH components separately, the atmosphere responds not to the individual components but rather to the total heating. As shown in Figure 9, the profile of maximum coherence from total heating tends to increase with altitude, with the exception of MC South and MC East for 100-hPa temperature. This suggests that, in general, both the warming (250 hPa) and cooling (100 hPa) signatures are more associated with heating aloft in the middle and upper troposphere. This would imply that the temperature responses depend on the vertical distribution of heating, if the high coherences do, in fact, depict the temperature responses due to the stationary KW/ERW signature. In the following discussion, we show that the vertical structure of coherences and time lags agrees well with those of KW/ERW responses found in previous studies.

The phases corresponding to the statistically significant coherences from total LH are shown in the left panel of Figure 10. Note that the phase plots are largely the same for total LH in the three layers above 6 km, while the lower two layers have typically low coherence (Figure 9). Hence, we show the phases from total LH inside 9–12 km since they are representative of the phase distribution in general. One common feature across all
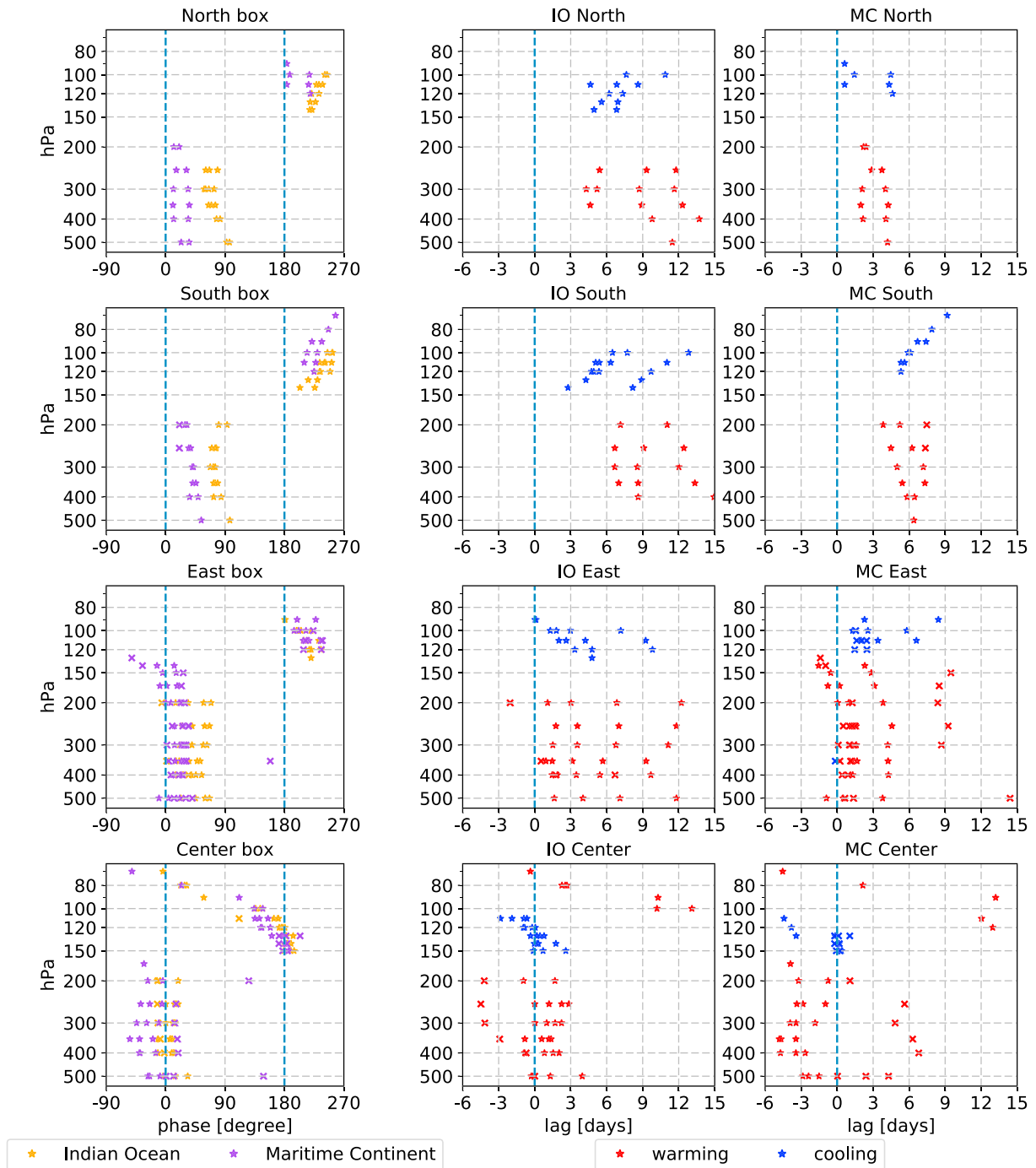
Figure 10. (Left) Phases corresponding to statistically significant coherences between 9–12 km total latent heating (LH) and temperature. Stars indicate that the time scale of the phase falls within 20–90 days, while the X marks phases outside this time scale. The ordinate axis denotes the pressure of the temperature time series. Positive phase indicates that the temperature lags LH. (Right) The lag in days, calculated from the phases in the left column. Positive lag indicates that temperature lags LH. Above 150 hPa, the 180° phase is assumed to be day 0 to estimate the lag of the cooling response (see text for explanation).

boxes in both regions is the shift from phases between 0° to 90° below ~150 hPa to phases larger than 180° above ~150 hPa. A 180° phase difference indicates that when the LH time series reaches a maximum in amplitude (in the given frequency f), the temperature reaches a minimum. Phases slightly larger than 180° indicate that the temperature reaches a minimum shortly after a peak in LH. For this reason, we interpret the phases distributed around 180° as the cooling response. Likewise, phases within 0° to 90° are interpreted to be the warming response. The vertical structure of the phases indicates that the variability of LH tends
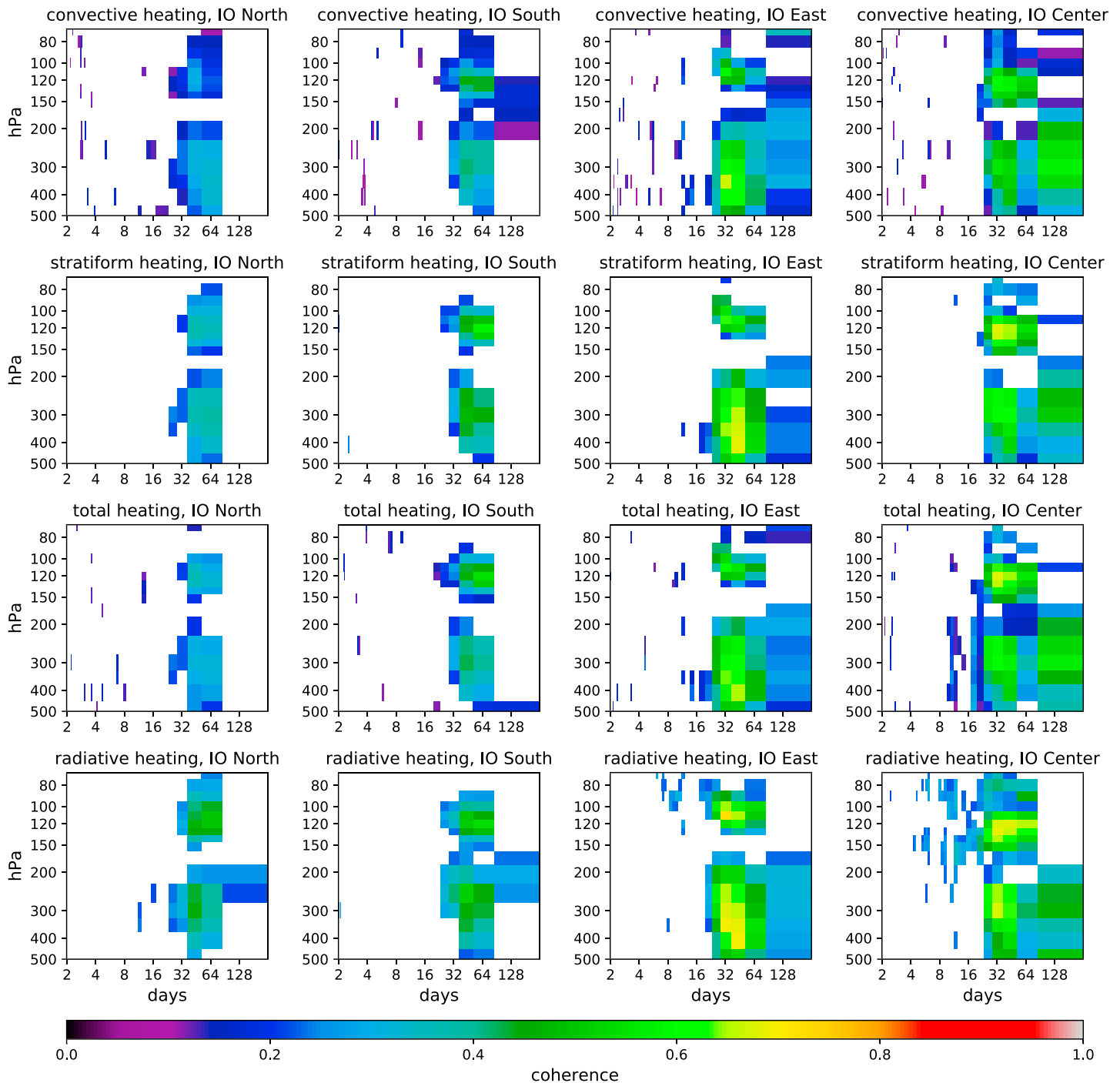
Figure 11. Highest coherence at each pressure level and frequency for convective (first row), stratiform (second row), total heating (third row), and radiative heating (fourth row) for the IO North, South, East, and Center boxes. The ordinate axis denotes the pressure of the temperature time series. White spaces indicate those pressures and frequency at which no coherences passed the significance testing. IO = Indian Ocean.

to be associated with cooling above 150 hPa and warming below, physically consistent with the equatorial planetary wave structure as found by Dima and Wallace (2007) who found that the largest geopotential height and wind anomalies due to equatorial planetary waves occur near 150 hPa.

The right panel of Figure 10 shows the time lag in days derived from the phase. Following the reasoning above, the lags above 150 hPa are calculated by assuming that day 0 is located at a phase of 180° in order to estimate the time lag of the cooling response, and below 150 hPa, the 0° phase is taken as day 0. In general,

inside the North, South, and East boxes, the lags fall within 0 to 12 days. Jin and Hoskins (1995) showed that in a model with prescribed heating, the ERW/KW response starts around day 3 after heating and ceases to change past 14 days. The lags found here are roughly consistent with this time range. In the North/South cases, the lags in the between 500 and 150 hPa are slightly larger than those above 150 hPa, suggesting that the upper-tropospheric warming response may be slightly slower than the TTL cooling response inside 80 to 150 hPa. Also, in IO North/South and MC South, the lags in the TTL clearly increase with height, although this feature is not present in MC North. This increase of lag with height may depict the upward propagation of the cold anomaly, which starts near 150 hPa where the geopotential anomalies occur.

The phases in the East boxes show signals of TTL cooling that is likely associated with KW, similar to the results of Zhou and Holton (2002) who concluded that intraseasonal cold temperature anomalies in these regions are likely due to KW excited by convection located west of these cold anomalies. Due to the eastward movement of MJO convection together with the eastward tilt of KW, it is expected that the phase of TTL cooling descends with time. This is seen in the phases of IO East which has a downward trend of phase in the cooling response. The IO Center has in addition a downward propagation of warming response from 70 to 100 hPa. This vertical structure is consistent with the KW associated with MJO convection (Figure 4 of Virts & Wallace, 2014), where the warming phase of the KW lies above the cooling phase. On the other hand, the downward propagation in MC Center is not very evident, and the phases in MC East show no signs of downward phase propagation.

Although the range of time lags found here are consistent with the response times found by Jin and Hoskins (1995), the positive time lags could also be due to the effects of MJO convection moving eastward rather than representing the response times of the atmosphere to the LH. The fact that anomalies associated with the MJO have a "swallowtail" shape (Zhang & Ling, 2011) means that the eastward movement of this anomaly may cause perturbations in the North/South boxes to lag that of the Center box. The East box would obviously be affected by eastward moving convection as well, as discussed above. Despite this possibility, the vertical structure of the warming and cooling is largely consistent with the known structure of equatorial waves, so the relationship between temperature and LH depicted here is most likely physical and still valuable for understanding which LH components are more highly associated with UTLS temperatures.

With this in mind, the distributions of these statistically significant coherences in all boxes are plotted in altitude and frequency space, as shown in Figure 11 for the IO region and Figure 12 for MC. In both regions, most statistically significant coherences fall within the time scales between 20 and 64 days, with much of the larger coherences (≥ 0.6) falling near 43 days. The maxima of coherences peak at time scales of ~43 days and, vertically, lie between 500 and 200 hPa. There is also a group of high coherences between 150 and 80 hPa, especially over IO. Most of the highest coherences therefore occur on time scales consistent with the MJO (20 to 90 days), suggesting that the observed coupling between temperature and LH is largely associated with the MJO. The importance of MJO on the intraseasonal time scale has been shown by Mote et al. (2000) who found that the MJO dominates the water vapor signal within 200 to 100 hPa and by Kim, Randel, and Birner (2018) who showed, through composites of water vapor fields with respect to MJO and non-MJO convection, that the dehydration signal is much stronger from convection associated with MJO. The results presented here further link these effects to LH associated with the MJO, since most statistically significant coherences occurs at MJO time scales. The collective results of this and existing studies suggest that MJO-associated convection has properties that set it apart from other convection in its ability to affect the UTLS through the planetary wave pattern.

Figure 13 contrasts the vertical profiles of coherence between temperature at each pressure level and convective/stratiform LH. At each pressure level, the temperature time series is paired with the LH time series from each of the five layers, and the maximum coherence (out of the five possible pairings) is plotted. The vertical distribution of coherences of convective and stratiform LH is very similar, since the two are highly correlated; stratiform precipitation often comes after convection. In the North and South boxes, the stratiform LH varies more coherently with temperatures throughout most of the TTL and upper troposphere. Near the tropopause (~100 hPa), the coherence from stratiform LH is higher than that of convective LH in all the North/South cases. This indicates that the TTL cooling is more closely related to stratiform LH. Similarly, in the upper troposphere (500 to 150 hPa), the higher coherences from stratiform LH shows a closer relationship between upper-tropospheric warming and stratiform LH. Coherences over IO North is lower, possibly due to the strong influences of off-equator heating from the Asian Monsoon during boreal sum-
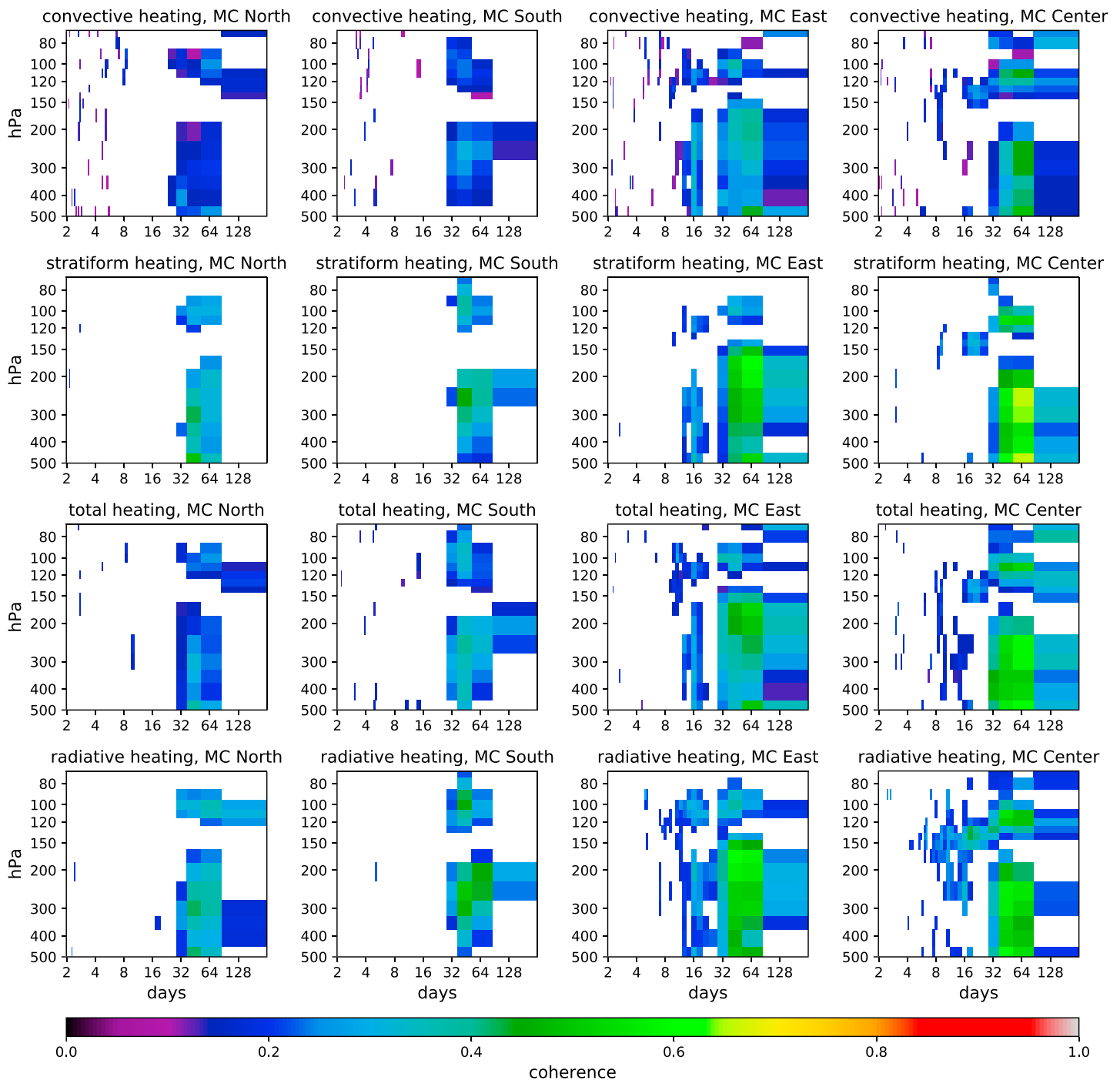
Figure 12. Same as Figure 11 except for the MC boxes. MC = Maritime Continent.

mer. Over the East boxes, coherences in the TTL are very close over IO, while over MC, the convective LH coherences are slightly larger. Stratiform coherences are larger at most altitudes below 150 hPa over the East boxes. These results show that upper-tropospheric warming has higher association with stratiform heating, and the same statement applies for TTL cooling, except for the MC East case.

Overall, our results show that (1) the upper-tropospheric warming and TTL cooling signal exhibit a dependence on heating altitude and (2) stratiform LH shares high coherences with TTL and upper-tropospheric temperature at MJO time scales. As noted in our previous discussion, the prominent effect of MJO on TTL water vapor and temperature is well-known. This study provides additional evidence that the mechanism
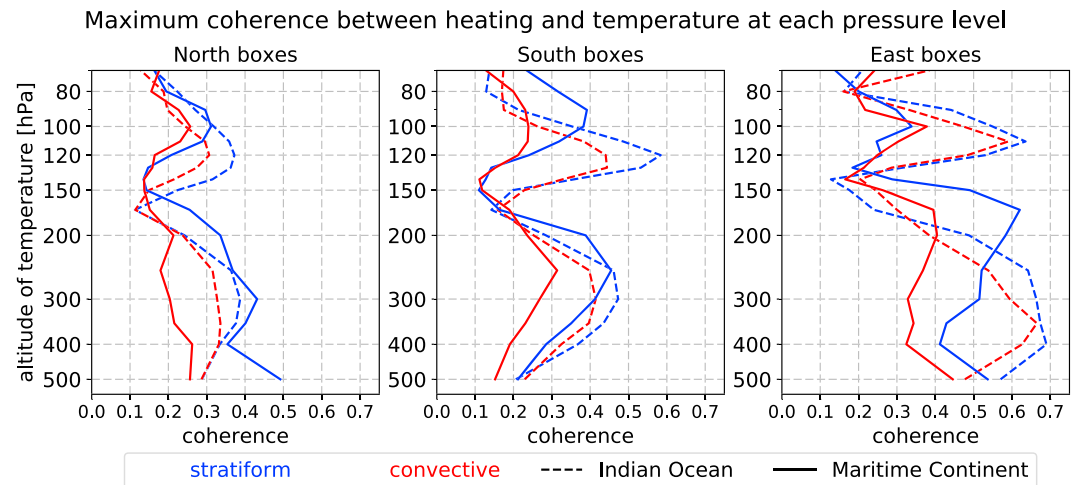
Figure 13. Profile of maximum coherence between temperature and latent heating for the North (left), South (middle), and East (right) boxes. The temperature time series from each pressure level (indicated by the ordinate axis) is paired with the latent heating time series from each of the five layers, and the coherence value plotted at each pressure represents the maximum coherence of the five possible pairings. Solid and dashed lines represent the Maritime Continent and Indian Ocean regions, respectively, while the colors distinguish the type of heating.

behind these effects is linked to the vertical structure of diabatic heating in the MJO. A distinct feature of MJO convection is its top-heavy heating profile as found in campaign observations (Kim, Zhang, et al., 2018; Lin et al., 2004) and cloud-permitting simulations (Wang et al., 2015). Based on our results, it is likely that the top-heavy heating of MJO convection is one of the factors that make it particularly effective in perturbing the UTLS. A physical explanation for stratiform LH being more important than convective LH for these UTLS signatures may be that the higher heating peaks place the perturbation anticyclones (see Figure 2) at higher altitudes. Another possibility is that the formation of stratiform precipitation usually implies a larger area of heating compared to convective precipitation which usually has vigorous vertical motion at smaller horizontal scales. It is also possible that stratiform precipitation and UTLS temperature perturbations are caused concurrently by large-scale circulations, resulting in high coherences between the two. Further studies would be necessary to understand the mechanisms connecting precipitation and UTLS temperature variability.

Aspects of the problem unaddressed with our approach include the dependence of the atmosphere's response in background flow varying with season. Since this study uses fixed box locations, it is unable to account for possible shifts in the position or vertical/horizontal tilt of the temperature perturbations. In addition, the coexistence of MJO and MCS makes it hard to separate the effects of moving convection and the dynamical response to diabatic heating, complicating the interpretation of the results. Our results here show a significant statistical relationship between stratiform LH and UTLS temperatures but cannot confirm whether this connection is causal.

5. Conclusion

This study examines the coupling between UTLS temperatures to tropical LH over the Indian Ocean and MC. With the goal of understanding whether the temperature perturbations depend on the vertical distribution of heating, we analyzed time series of LH spanning from 0 to 15 km in altitude and time series of temperature from 500 to 70 hPa. The spectral coherence and phase, derived from cross-spectral analysis, were studied to understand the role of heating altitude and contribution of convective/stratiform heating to the temperature variations. Statistically significant coherences between total heating and temperature are generally higher when total heating occurred above 6 km, signifying that the TTL cooling and upper-tropospheric warming are related to the heating altitude. Analysis of the phase and lag between temperature and LH shows that the vertical structure and time scale of the lags between LH and temperature agree well with previous studies of equatorial waves, suggesting that the coherence observed between LH and UTLS temperatures likely depict the coupling through planetary waves. The coherence between temper-

atures and total LH increased with the altitude of LH. This increase of coherence values with height suggests that LH occurring at higher altitudes may favor the formation of the horseshoe cold trap over the MC or that the UTLS temperature perturbations are coupled to circulations that form precipitation at higher altitudes.

Stratiform LH, which is characterized by a higher heating peak altitude, was found to have higher coherences overall with UTLS temperatures. In all the studied cases, the stratiform LH coherences associated with the TTL cooling in the tail region (North/South boxes) of the horseshoe are higher than those of convective LH. On the other hand, the coherences associated with the KW cooling showed negligible difference between convective and stratiform LH. Possible explanations for this results could be that stratiform LH is more effective at forming the tails of the cold trap or that the large-scale circulations responsible for the tail formation is closely associated with stratiform LH. Further exploring this connection may provide some insight into why the winter temperature climatology of some climate models (e.g., Gettelman & Birner, 2007) captures the cold trap but without pronounced tails. Improved modeling in the vertical distribution of LH as well as the partitioning between convective and stratiform LH may increase the accuracy of the TTL in models.

In the frequency domain, most statistically significant coherences between UTLS temperature and LH fall within the time scale of 20 to 64 days, which corresponds roughly to the MJO time scale of 20 to 90 days. The fact that most high coherence values occurred at MJO time scales, together with the findings of Kim, Randel, and Birner (2018) which found that MJO convection causes more pronounced dehydration than non-MJO convection, suggests that MCS in the MJO exert strong influence on TTL cooling and subsequent dehydration processes. Based on results of this study, we suggest that the top-heaviness of heating in the MJO at least partially plays a role in its prominent signal in TTL and upper-tropospheric water vapor and temperature as shown here and in previous studies.

References

Anthes, R. A., Bernhardt, P. A., Chen, Y., Cucurull, L., Dymond, K. F., Ector, D., et al. (2008). The COSMIC/FORMOSAT-3 Mission: Early results. *Bulletin of the American Meteorological Society*, *89*(3), 313–334. https://doi.org/10.1175/BAMS-89-3-313

Awaka, J., Iguchi, T., Kumagai, H., & Okamoto, K. (2002). Rain type classification algorithm for TRMM Precipitation Radar, *Proc. ieee igarss* (Vol. 4, pp. 1633–1635). Singapore: IEEE. https://doi.org/10.1109/IGARSS.1997.608993

Biltoft, C. A., & Pardyjak, E. R. (2009). Spectral coherence and the statistical significance of turbulent flux computations. *Journal of Atmospheric and Oceanic Technology*, *26*(2), 403–409. https://doi.org/10.1175/2008JTECHA1141.1

Bretherton, C. S., Widmann, M., Dymnikov, V. P., Wallace, J. M., & Bladé, I. (1999). The effective number of spatial degrees of freedom of a time-varying field. *Journal of Climate*, *12*(7), 1990–2009. https://doi.org/10.1175/1520-0442(1999)012<1990:TENOSD>2.0.CO;2

Dima, I. M., & Wallace, J. M. (2007). Structure of the annual-mean equatorial planetary waves in the ERA-40 reanalyses. *Journal of the Atmospheric Sciences*, *64*(8), 2862–2880. https://doi.org/10.1175/JAS3985.1

Doelling, D. R., Sun, M., Nguyen, L. T., Nordeen, M. L., Haney, C. O., Keyes, D. F., & Mlynczak, P. E. (2016). Advances in geostationary-derived longwave fluxes for the CERES synoptic (SYN1deg) Product. *Journal of Atmospheric and Oceanic Technology*, *33*(3), 503–521. https://doi.org/10.1175/JTECH-D-15-0147.1

Foelsche, U., Scherllin-Pirscher, B., Ladstädter, F., Steiner, A. K., & Kirchengast, G. (2011). Refractivity and temperature climate records from multiple radio occultation satellites consistent within 0.05%. *Atmospheric Measurement Techniques*, *4*(9), 2007–2018. https://doi.org/10.5194/amt-4-2007-2011

Forster, P. M. D. F., & Shine, K. P. (1999). Stratospheric water vapour changes as a possible contributor to observed stratospheric cooling. *Geophysical Research Letters*, *26*(21), 3309–3312. https://doi.org/10.1029/1999GL010487

Fueglistaler, S. (2005). Stratospheric water vapor predicted from the Lagrangian temperature history of air entering the stratosphere in the tropics. *Journal of Geophysical Research*, *110*, D08107. https://doi.org/10.1029/2004JD005516

Gettelman, A., & Birner, T. (2007). Insights into tropical tropopause layer processes using global models. *Journal of Geophysical Research*, *112*(23), 1–15. https://doi.org/10.1029/2007JD008945

Gill, A. E. (1980). Some simple solutions for heat induced tropical circulation. *Quarterly Journal of the Royal Meteorological Society*, *106*(449), 447–462. https://doi.org/10.1002/qj.49710644905

Hagos, S., Zhang, C., Tao, W.-K., Lang, S., Takayabu, Y. N., Shige, S., et al. (2010). Estimates of tropical diabatic heating profiles: Commonalities and uncertainties. *Journal of Climate*, *23*(3), 542–558. https://doi.org/10.1175/2009JCLI3025.1

Highwood, E. J., & Hoskins, B. J. (1998). The tropical tropopause. *Quarterly Journal of the Royal Meteorological Society*, *124*(549), 1579–1604. https://doi.org/10.1002/qj.49712454911

Houze, R. a. Jr. (2004). Mesoscale convective systems. *Reviews of Geophysics*, *42*, RG4003. https://doi.org/10.1029/2004RG000150

Iguchi, T., Meneghini, R., Awaka, J., Kozu, T., & Okamoto, K. (2000). Rain profiling algorithm for TRMM Precipitation Radar data. *Advances in Space Research*, *25*(5), 973–976. https://doi.org/10.1016/S0273-1177(99)00933-3

Jensen, E. J., Toon, O. B., Pfister, L., & Selkirk, H. B. (1996). Dehydration of the upper troposphere and lower stratosphere by subvisible cirrus clouds near the tropical tropopause. *Geophysical Research Letters*, *23*(8), 825–828. https://doi.org/10.1029/96GL00722

Jin, F., & Hoskins, B. J. (1995). The direct response to tropical heating in a baroclinic atmosphere. *Journal of the Atmospheric Sciences*, *52*(3), 307–319. https://doi.org/10.1175/1520-0469(1995)052<0307:TDRTTH>2.0.CO;2

Kim, J., Randel, W. J., & Birner, T. (2018). Convectively driven tropopause-level cooling and its influences on stratospheric moisture. *Journal of Geophysical Research: Atmospheres*, *123*, 590–606.https://doi.org/10.1002/2017JD027080

Kim, J.-E., Zhang, C., Kiladis, G. N., & Bechtold, P. (2018). Heating and moistening of the MJO during DYNAMO in ECMWF reforecasts. *Journal of the Atmospheric Sciences*, *75*(5), 1429–1452. https://doi.org/10.1175/JAS-D-17-0170.1

Kummerow, C., Barnes, W., Kozu, T., Shiue, J., & Simpson, J. (1998). The Tropical Rainfall Measuring Mission (TRMM) sensor package. *Journal of Atmospheric and Oceanic Technology*, *15*(3), 809–817. https://doi.org/10.1175/1520-0426(1998)015<0809:TTRMMT>2.0.CO;2

Kursinski, E. R., Hajj, G. A., Schofield, J. T., Linfield, R. P., & Hardy, K. R. (1997). Observing Earth's atmosphere with radio occultation measurements using the global positioning system. *Journal of Geophysical Research*, *102*(D19), 23,429–23,465. https://doi.org/10.1029/97JD01569

L'Ecuyer, T. S., & Mcgarragh, G. (2010). A 10-year climatology of tropical radiative heating and its vertical structure from TRMM observations. *Journal of Climate*, *23*(3), 519–541. https://doi.org/10.1175/2009JCLI3018.1

Lin, J., Mapes, B., Zhang, M., & Newman, M. (2004). Stratiform precipitation, vertical heating profiles, and the Madden–Julian Oscillation. *Journal of the Atmospheric Sciences*, *61*(3), 296–309. https://doi.org/10.1175/1520-0469(2004)061<0296:SPVHPA>2.0.CO;2

Matsuno, T. (1966). Quasi-geostrophic motions in the equatorial area. *Journal of the Meteorological Society of Japan. Ser. II*, *44*(1), 25–43. https://doi.org/10.2151/jmsj1965.44.1_25

Mote, P. W., Clark, H. L., Dunkerton, T. J., Harwood, R. S., & Pumphrey, H. C. (2000). Intraseasonal variations of water vapor in the tropical upper troposphere and tropopause region. *Journal of Geophysical Research*, *105*(D13), 17,457–17,470. https://doi.org/10.1029/2000JD900158

Mote, P. W., Rosenlof, K. H., McIntyre, M. E., Carr, E. S., Gille, J. C., Holton, J. R., et al. (1996). An atmospheric tape recorder: The imprint of tropical tropopause temperatures on stratospheric water vapor. *Journal of Geophysical Research*, *101*(D2), 3989. https://doi.org/10.1029/95JD03422

Nesbitt, S. W., Cifelli, R., & Rutledge, S. A. (2006). Storm morphology and rainfall characteristics of TRMM precipitation features. *Monthly Weather Review*, *134*(10), 2702–2721. https://doi.org/10.1175/MWR3200.1

Nishimoto, E., & Shiotani, M. (2012). Seasonal and interannual variability in the temperature structure around the tropical tropopause and its relationship with convective activities. *Journal of Geophysical Research*, *117*, 1–11. https://doi.org/10.1029/2011JD016936

Paulik, L. C., & Birner, T. (2012). Quantifying the deep convective temperature signal within the tropical tropopause layer (TTL). *Atmospheric Chemistry and Physics*, *12*(24), 12,183–12,195. https://doi.org/10.5194/acp-12-12183-2012

Rind, D., & Lonergan, P. (1995). Modeled impacts of stratospheric ozone and water vapor perturbations with implications for high-speed civil transport aircraft. *Journal of Geophysical Research*, *100*(D4), 7381–7396. https://doi.org/10.1029/95JD00196

Ryu, J.-H., Lee, S., & Son, S.-W. (2008). Vertically propagating Kelvin waves and tropical tropopause variability. *Journal of the Atmospheric Sciences*, *65*(6), 1817–1837. https://doi.org/10.1175/2007JAS2466.1

Schumacher, C., & Houze, R. A. (2003). The TRMM Precipitation Radar's view of shallow, isolated rain. *Journal of Applied Meteorology*, *42*(10), 1519–1524. https://doi.org/10.1175/1520-0450(2003)042<1519:TTPRVO>2.0.CO;2

Shige, S., Takayabu, Y. N., Kida, S., Tao, W.-K., Zeng, X., Yokoyama, C., & L'Ecuyer, T. (2009). Spectral retrieval of latent heating profiles from TRMM PR data. Part IV: Comparisons of lookup tables from two- and three-dimensional cloud-resolving model simulations. *Journal of Climate*, *22*(20), 5577–5594. https://doi.org/10.1175/2009JCLI2919.1

Shige, S., Takayabu, Y. N., & Tao, W. K. (2008). Spectral retrieval of latent heating profiles from TRMM PR data. Part III: Estimating apparent moisture sink profiles over tropical oceans. *Journal of Applied Meteorology and Climatology*, *47*(2), 620–640. https://doi.org/10.1175/2007JAMC1738.1

Shige, S., Takayabu, Y. N., Tao, W.-K., & Shie, C.-L. (2007). Spectral retrieval of latent heating profiles from TRMM PR data. Part II: Algorithm improvement and heating estimates over tropical ocean regions. *Journal of Applied Meteorology and Climatology*, *46*(7), 1098–1124. https://doi.org/10.1175/JAM2510.1

Shige, S., Takayabu, Y. N., Tao, W.-K., & Johnson, D. E. (2004). Spectral retrieval of latent heating profiles from TRMM PR data. Part I: Development of a model-based algorithm. *Journal of Applied Meteorology*, *43*(8), 1095–1113. https://doi.org/10.1175/1520-0450(2004)043<1095:SROLHP>2.0.CO;2

Simpson, J., Adler, R. F., & North, G. R. (1988). A proposed Tropical Rainfall Measuring Mission (TRMM) Satellite. *Bulletin of the American Meteorological Society*, *69*(3), 278–295. https://doi.org/10.1175/1520-0477(1988)069<0278:APTRMM>2.0.CO;2

Solomon, S., Kiehl, J. T., Garcia, R. R., & Grose, W. (1986). Tracer transport by the diabatic circulation deduced from satellite observations. *Journal of Atmospheric Sciences*, *43*(15), 1603–1642. https://doi.org/10.1175/1520-0469(1986)043<1603:TTBTDC>2.0.CO;2

Tao, W.-K., Lang, S., Simpson, J., & Adler, R. (1993). Retrieval algorithms for estimating the vertical profiles of latent heat release: Their applications for TRMM. *Journal of the Meteorological Society of Japan. Ser. II*, *71*(December), 685–700.

Tao, W. K., Lang, S., Zeng, X., Shige, S., & Takayabu, Y. (2010). Relating convective and stratiform rain to latent heating. *Journal of Climate*, *23*(7), 1874–1893. https://doi.org/10.1175/2009JCLI3278.1

Tao, W.-K., & Simpson, J. (1993). Goddard cumulus ensemble model. Part I: Model description. *Terrestrial Atmospheric and Oceanic Sciences*, *4*(1), 035. https://doi.org/10.3319/TAO.1993.4.1.35(A)

Tao, W.-K., Takayabu, Y. N., Lang, S., Shige, S., Olson, W., Hou, A., et al. (2016). TRMM latent heating retrieval: Applications and comparisons with field campaigns and large-scale analyses. *Meteorological Monographs*, *56*(Code 612), 2.1–2.34. https://doi.org/10.1175/AMSMONOGRAPHS-D-15-0013.1

Virts, K. S., & Wallace, J. M. (2014). Observations of temperature, wind, cirrus, and trace gases in the tropical tropopause transition layer during the MJO. *Journal of the Atmospheric Sciences*, *71*(3), 1143–1157. https://doi.org/10.1175/JAS-D-13-0178.1

Von Engeln, A., Healy, S., Marquardt, C., Andres, Y., & Sancho, F. (2009). Validation of operational GRAS radio occultation data. *Geophysical Research Letters*, *36*, L17809. https://doi.org/10.1029/2009GL039968

Wang, S., Sobel, A. H., Zhang, F., Sun, Y. Q., Yue, Y., & Zhou, L. (2015). Regional simulation of the October and November MJO events observed during the CINDY/DYNAMO field campaign at gray zone resolution. *Journal of Climate*, *28*(6), 2097–2119. https://doi.org/10.1175/JCLI-D-14-00294.1

Welch, P. (1967). The use of fast Fourier transform for the estimation of power spectra: A method based on time averaging over short, modified periodograms. *IEEE Transactions on Audio and Electroacoustics*, *15*(2), 70–73. https://doi.org/10.1109/TAU.1967.1161901

Wickert, J., Reigber, C., Beyerle, G., König, R., Marquardt, C., Schmidt, T., et al. (2001). Atmosphere sounding by GPS radio occultation: First results from CHAMP. *Geophysical Research Letters*, *28*(17), 3263–3266. https://doi.org/10.1029/2001GL013117

Yanai, M., Esbensen, S., & Chu, J.-H. (1973). Determination of bulk properties of tropical cloud clusters from large-scale heat and moisture budgets. *Journal of the Atmospheric Sciences*, *30*(4), 611–627. https://doi.org/10.1175/1520-0469(1973)030<0611:DOBPOT>2.0.CO;2

Zhang, C., & Ling, J. (2011). Potential vorticity of the Madden–Julian Oscillation. *Journal of the Atmospheric Sciences*, *69*(1), 65–78. https://doi.org/10.1175/jas-d-11-081.1

Zhou, X., & Holton, J. R. (2002). Intraseasonal variations of tropical cold-point tropopause temperatures. *Journal of Climate*, *15*(12), 1460–1473. https://doi.org/10.1175/1520-0442(2002)015<1460:IVOTCP>2.0.CO;2